

Microtubule Structure at 8 Å Resolution

Huilin Li,¹ David J. DeRosier,^{1,4}
William V. Nicholson,¹ Eva Nogales,^{1,2}
and Kenneth H. Downing^{1,3}

¹Life Sciences Division

Lawrence Berkeley National Laboratory
Berkeley, California 94720

²Howard Hughes Medical Institute
Department of Molecular and Cell Biology
University of California, Berkeley
Berkeley, California 94720

Summary

We have obtained a 3D reconstruction of intact microtubules, using cryoelectron microscopy and image processing, at a resolution of about 8 Å, sufficient to resolve much of the secondary structure. The level of detail in the map allows docking of the tubulin structure previously determined by electron crystallography, with very strong constraints, providing several important insights not previously available through docking tubulin into lower-resolution maps. This work provides an improved picture of the interactions between adjacent protofilaments, which are responsible for microtubule stability, and also suggests that some structural features are different in microtubules from those in the zinc sheets with which the tubulin structure was determined.

Introduction

Microtubules play fundamental roles throughout the life of eukaryotic cells. These roles often depend on the dynamic instability of microtubules and its regulation by cellular factors. The dynamic behavior of microtubules has been the subject of great interest for several decades, but only recently has the structure of tubulin allowed us to begin to understand the molecular basis of the dynamics [1]. In order to advance our knowledge of the regulation of the microtubule cytoskeleton, we must develop a better understanding of the interactions among the tubulin subunits within a microtubule. The structure of the intact microtubule that we report on here reveals new information about the interprotein interactions and conformational features associated with the formation of microtubules.

The structural unit of a microtubule is the α - β tubulin heterodimer. The structure of the dimer was determined by electron crystallography with crystalline sheets of tubulin that form in the presence of zinc ions [2] and has recently been refined to 3.5 Å resolution [3]. Alpha and β tubulins share about 40% sequence homology, and, as expected, their structures are very similar. In-

deed, at a resolution around 6 Å, the structures appear essentially indistinguishable [4], although, at higher resolution, differences in side chains and some differences in secondary structure are identified.

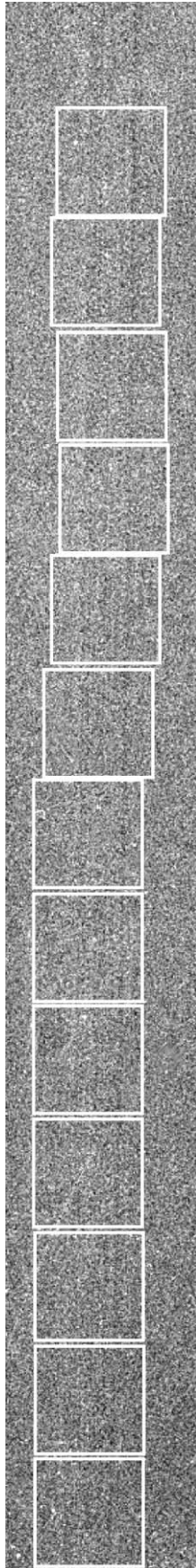
Dimers connect head to tail to form protofilaments (pf), and protofilaments assemble side by side to form the microtubule. Both in vivo and (under some conditions) in vitro, most microtubules have 13 protofilaments, although this number can vary from 9 to 16 [5]. The protofilaments follow a helical path around the microtubule axis with a long pitch, often called the superhelix, but, in microtubules with 13 protofilaments, they are essentially parallel to the microtubule axis, with no helical twist. This special feature is exploited in our microtubule image processing procedure. The monomers follow a shallow, left-handed helix. In most microtubule types, including those with 13 protofilaments, this helix rises by three monomers in one turn around the axis, producing what is termed a three-start helix. Since the rise corresponds to one and a half dimers, there is a seam running along the length of the microtubule where different types of monomers become neighbors. Thus, 13 pf microtubules are not strictly helical in the sense of all heterodimers being related by the helical symmetry. In fact, only a few of the naturally occurring microtubule types, such as 12 pf, two-start types and 15 and 16 pf, four-start types, have such symmetry and are amenable to helical image processing. If the differences between α and β are ignored, though, all microtubules can be considered true helices. The 13 pf microtubules, though, are degenerate helices, as their protofilaments run parallel to the axis. The Fourier transform of a helix consists of a set of layer lines, each populated with a set of Bessel functions that derive from the helix structure. In conventional helical image processing, values for the Bessel functions are determined from Fourier transforms of images and are used to compute the helix structure. In the case of 13 pf microtubules, however, layer lines contain overlapping Bessel functions of different order. This adds a degree of complication in analyzing images by helical methods.

Helical methods have been used with notable success in reconstructing microtubules and motor-decorated microtubules [6–10], although the resolution has generally been limited to 15–20 Å. Back projection methods have also been used for generating reconstructions of motor-decorated microtubules [11, 12]. The helical nature of the microtubule provides a series of views from different angles that can be used to produce a 3D representation from a single image, but without imposing helical symmetry. While this approach has even allowed the identification of the seam in some of the nonhelical microtubule types, it has not yet yielded higher resolution than the helical methods.

Structural information about the lateral contacts between protofilaments is of special importance in under-

³Correspondence: kdowning@lbl.gov

⁴Present address: Department of Biology and The Rosenstiel Basic Medical Sciences Research Center, Brandeis University, Waltham, Massachusetts 02454.



standing the dynamics and regulation of microtubule assembly and disassembly. In particular, disassembly of the microtubule is generally understood to result from a weakening of the lateral interactions, and we would like to understand in detail both the nature of these interactions and their possible transitions. The atomic structure of tubulin, which was determined from two-dimensional crystals of protofilaments, did not provide information about the lateral interactions between protofilaments in microtubules. In the crystals, the protofilaments are antiparallel, whereas, in microtubules, they are parallel. While the longitudinal, intraprotofilament interactions in the two structures are assumed to be the same, the lateral interactions between the protofilaments must be completely different. In addition, there may also be conformational differences in tubulin between the two polymers. We obtained a first model of the microtubule by docking the atomic structure of the protofilament into a microtubule reconstruction that had a nominal resolution of about 20 Å [13]. The fit of the model within the molecular envelope was very good, giving information about the relative orientations and interactions between adjacent dimers. More recently, reconstructions at higher resolution [10, 14] allowed some refinement of the docking. However, none of these reached the sub-10 Å resolution necessary to identify elements of secondary structure and, thereby, to characterize conformational differences between the zinc sheet and microtubule protofilaments.

Advances in the methodology of single-particle reconstructions have made it feasible to consider this approach to obtaining resolution better than 10 Å with microtubules, by treating each image as a string of single particles. This approach allows one to take account of distortions within a single microtubule that limit resolution with helical processing. Using a combination of single-particle and crystallographic image processing methods, we have obtained a microtubule reconstruction at 8 Å resolution. Most of the α helices in the dimer structure can be identified in this map, providing a very strong constraint in placement of the atomic structure. This docking gives an improved picture of the interprotofilament interactions and suggests some conformational differences in tubulin between microtubules and Zn sheets.

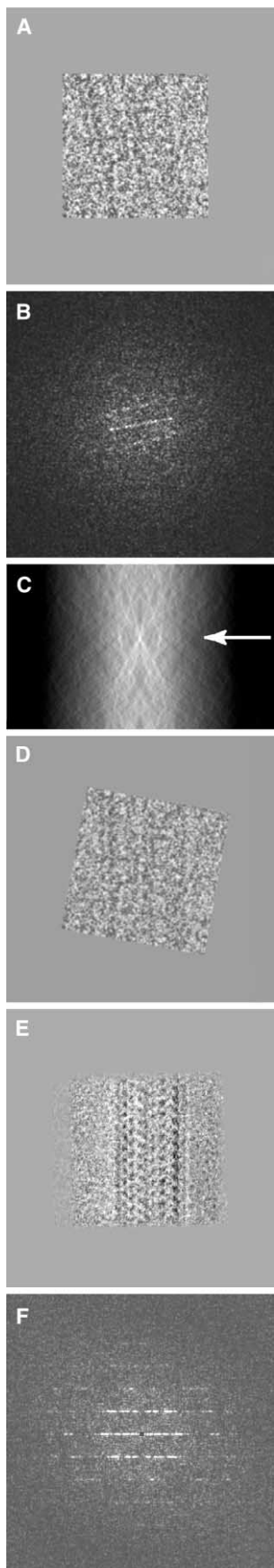
Results

Microtubule Images and CTF Determination

The selection of microtubules with a defined number of protofilaments from images of ice-embedded samples is fairly straightforward when the defocus is high enough to give maximum contrast. The superposition of protofilaments on the top and bottom of a microtubule produces a distinctive moiré pattern in the projection image that can be used to determine the type of most microtu-

Figure 1. Part of a Typical Microtubule Image, Recorded with a Defocus of about 1 μm

Boxes indicate 320 \times 320 pixel segments that have been cut out of the image.



bules [5]. However, the contrast in our low-defocus images recorded at 400 kV (Figure 1) is too low to allow visual identification of the microtubule type, so selection was based on optical Fourier transforms. Generally, the selection process emphasized the strength and completeness of the second layer line, corresponding to 20 Å resolution. In the best images, the optical diffraction extended to the fourth layer line at 10 Å resolution. In principle, the lack of layer line splitting in the off-meridional part of the Fourier transform, corresponding to the moiré pattern in the image, should be sufficient to identify the 13-protofilament microtubules. However, there was not always a sufficient signal to noise ratio to eliminate non-13-protofilament microtubules, and there were occasional transitions in the number of protofilaments along a single microtubule, as well as other defects [15]. Thus, a second selection was performed on the microtubules after digitization: the images were compressed by a factor of four along the axis and filtered to enhance the visibility of the protofilaments in order to judge by eye whether they contained 13 protofilaments along the entire length.

Correction for the sign of the contrast transfer function (CTF) was done before image alignment. The CTF was determined by first adding the power spectra for all of the segments along a single microtubule. The resulting power spectrum was band-pass filtered, and a plot of the radial average was then fit to a curve representing the CTF. The error in the defocus is estimated to be less than 500 Å, providing an accurate determination of the CTF out to about 7 Å resolution.

Rotational Alignment, Magnification Scaling, and Segment Averaging

Even in the best images, the microtubules undergo a significant in-plane curvature that must be corrected before combining segments. For most helical image processing, this is done by fitting a curve along the center of the object and then straightening the image by interpolation on the basis of a spline fit to the curve [16]. Our approach was to rotationally align each short segment individually. We found that we could efficiently deter-

Figure 2. Alignment by Radon Transform

- (A) Original image segment.
- (B) Power spectrum of (A)
- (C) Radon transform [17, 18] of power spectrum. The discrete Radon transform is a series of projections along different angles. Each horizontal row in the transform (C) corresponds to the projection of the power spectrum (B) along one direction. With a helical specimen, projection of the power spectrum along the direction of the layer lines produces a set of distinct peaks that are identified with a high signal to noise ratio. Only in the direction perpendicular to the microtubule axis, corresponding to the row of the transform marked by the arrow, does the projection have a maximum at the central position. A simple peak centroid search along the central column gives the in-plane rotation angle. Peaks also arise from the higher-order layer lines and are used for magnification scaling. If these peaks are not clear enough or are more than a preset limit from the expected positions, the segment is rejected.
- (D) Segment after rotational alignment
- (E) Average of 28 aligned segments from the micrograph shown in Figure 1.
- (F) Power spectrum of (E).

mine the orientation to within 0.5° using a Radon transform [17, 18] of the power spectrum of the segment. As illustrated in Figure 2, the layer lines in the Fourier transform of each segment give rise to distinct spots on the Radon transform that can be used to determine both the in-plane rotation and magnification scaling.

If there is no significant variation in the out of plane tilt or axial twist of the microtubule within each image, the rotationally aligned segments can be translationally aligned by crosscorrelation and then averaged to produce an image with good signal to noise ratio. One such average of 28 segments from the microtubule shown in Figure 1 and its Fourier transform are shown in Figures 2E and 2F. Many structural details are visible in this picture, and, in the Fourier transform of the average, there is an identifiable signal up to the fourth layer line, with isotropic resolution to at least 10 \AA . However, variations in the out of plane tilt and axial twist prevented obtaining resolution much beyond 10 \AA .

Reference-Based Alignment

In order to identify the precise orientation of each segment, we turned to a multireference-based alignment scheme [19]. Given knowledge of the crystallographic structure of the tubulin dimer and a fair idea of how it fits into the microtubule, we had an opportunity to construct a microtubule reference using the atomic model, with the caveat that we had to ensure that this reference would not bias the reconstruction. We assume that the protofilament structure observed in the crystals is the same as in the microtubules, at least at the current resolution, so that the only two free parameters to be determined in constructing the reference are the radius at which the dimer sits and its rotational angle about the protofilament axis. The procedure used for determining these parameters and producing the reference is as follows.

From each of the first 14 microtubule images selected for processing, we constructed individual 3D density maps by back projection. Each map was produced by generating 13 copies of the averaged, CFT-corrected segment image from a given microtubule to represent the 13 symmetry-related views, with axial shifts to account for the rise after each 13-fold rotational operation. The averaged image of each microtubule had very good contrast and could be roughly centered by visual inspection. This centering was refined manually after examining the resultant 3D map (if the image is not exactly centered on the axis, the reconstruction will have high density in the middle, where it should be featureless). This method is objective, as the maps were not affected in any way by reference models. The correct protofilament radius was obtained by visually comparing each map with a series of microtubule models that were calculated with the crystal structure placed at different radii. The average radius to the dimer center of mass in these 14 reconstructions was 112 \AA .

In order to determine the protofilament rotational angle, we constructed a series of reference models by placing the crystal structure at the average radius, at different angles around the protofilament axis. The crosscorrelation was computed between projections of

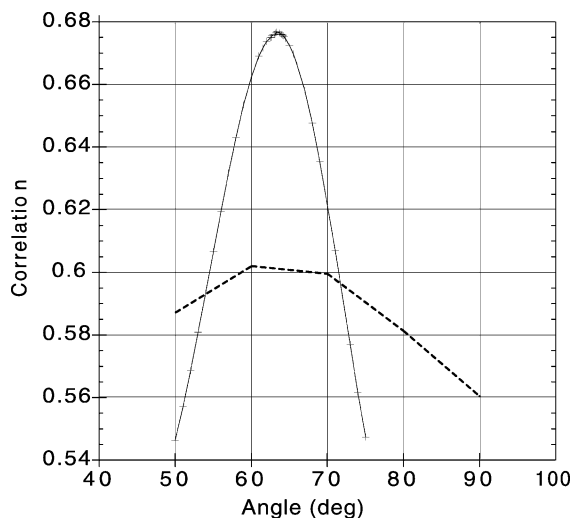


Figure 3. Correlations between Experimental Maps and Models Constructed from the Atomic Structure of Tubulin

The dotted curve represents the average correlation between the first 14 microtubule images processed and projections of microtubule models, which were built with the crystal structure at different rotation angles around the protofilament axis. The solid curve shows the correlation between the final microtubule map and a 3D density map calculated from the crystal structure of the dimer, computed as in [11], as the dimer density is rotated about the protofilament axis.

each of these models and the averages of the 14 microtubule images. As shown in Figure 3, the correlation function showed a clear peak at an angle close to that determined in the original docking [13]. We used the model that gave the best correlation to generate a set of reference images for the multireference alignment.

The reference images were calculated by projecting the model. Projections were taken at 1° intervals, covering a range of axial rotational angles of $1/13$ of a full rotation ($\sim 28^\circ$) and out of plane tilt angles from -10° to $+10^\circ$. At this stage, each individual segment was averaged and reduced to the length of just two monomers by superimposing 13 copies of the image with axial shifts of one monomer and then cutting out a section two monomers long from the middle of the resultant image. This step made subsequent computational steps substantially faster. Translational parameters and Eulerian angles were obtained for each of the segments from the maximum correlation with the reference projection set.

One objective criterion that can be used to validate the alignment procedure is that both the rotational and tilt angles should change slowly and continuously along the microtubule axis. Almost all adjacent segments were found to be within 2° of each other, but, on occasion, the difference was significantly larger, apparently because of a failure of the alignment. We set a limit of 3° for the difference in orientation between adjacent segments and excluded those segments whose alignment was not consistent with their neighbors. This procedure resulted in rejection of about 300 of the initial 1500 segments.

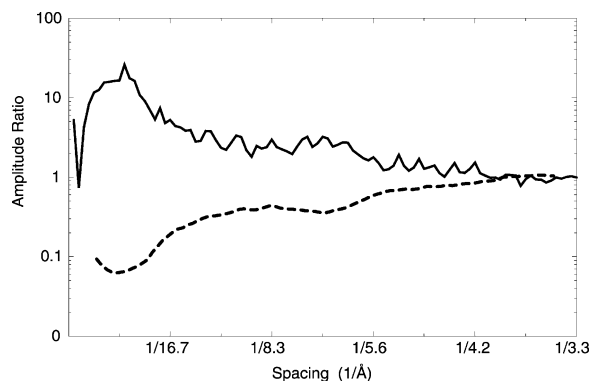


Figure 4. Scaling of Fourier Transform

The solid curve shows the ratio of averaged transform amplitudes from projections of the map to amplitudes from corresponding projections of the reference model that was derived from the tubulin crystal structure. The dotted curve is the reciprocal of a ten-point running averaging of the projection ratio curve and was used to scale the transform of the microtubule map with a low pass filter that removed frequencies above ~ 7 Å.

The Microtubule Map at 8 Å Resolution

Data from 89 microtubule images, comprising 1,200 segments and about 200,000 monomers, were combined to produce the final map. About half of the selected microtubules had orientation angles around the axis within 2° of either 0° or 14° , since these angles produce the most symmetric diffraction and were thus strongly favored in the selection process. The rest were uniformly distributed in the rest of the 0° – 28° range. The map calculation was performed in two steps, avoiding the need to generate the 13 equivalent views for each segment. First, back projection was used to reconstruct a map with information from only the angular range from 0° to 28° around the axis. This map was then symmetrized according to the 13-fold helical operation that places one monomer $40.6/13$ Å along the axis from the previous one, with a rotation of $4 \times 360^\circ/13^\circ$ around the axis. Iterative refinement is a standard part of single-particle work, but two more cycles of correlation with new reference projections from the previous cycle maps did not result in significant change or improvement. The failure of the map to improve with this type of refinement is understandable, as we started out with a very good microtubule model based on the crystal structure.

In order to determine an appropriate curve for scaling the Fourier transform of the reconstruction to compensate for the normal resolution-dependent falloff in amplitudes, we compared the Fourier transforms of several sections and projections of the map and the reference built from the crystal structure of tubulin. The results are shown in Figure 4. The solid curve is the ratio of amplitudes from projections of the map and model. Ratios of x and z sections gave essentially identical curves. The peak in the 20–30 Å-resolution range and the low value near the origin arise from the average CTF of the images used, with CTF oscillations at higher resolution washed out by the variations in defocus among the images. Because the data for the curve come from the relatively small number of points along the layer lines in the Fourier transform, this curve is noticeably noisier

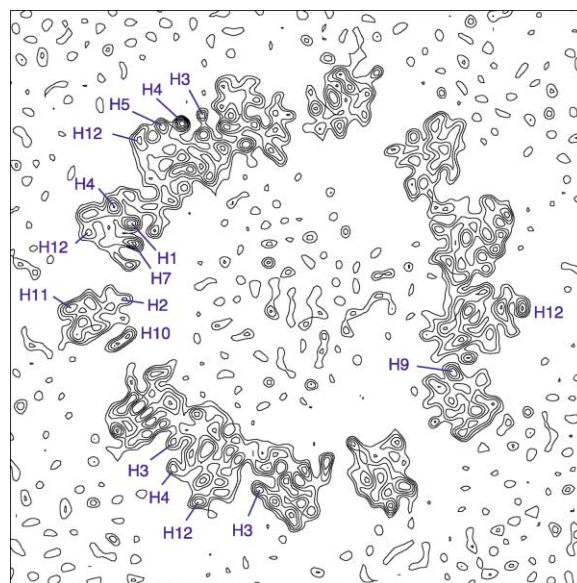


Figure 5. Contour Plot of One Section of the Microtubule Density Map

The section cuts through adjacent monomers 9.4 Å apart along the axis and is viewed looking from the plus end toward the minus end. Positions of several of the α helices in the crystal structure are marked.

than comparable curves shown in similar work [20]. The dotted curve is the reciprocal of a ten-point running average of the projection ratio (solid) curve and was used to scale the microtubule map, with a low-pass filter that effectively removed frequencies above ~ 7 Å. Over the resolution range from about 40 to 8 Å, the falloff can be approximated by a function of the form $\exp(-B/d^2)$, with $B = 75 \text{ Å}^2$, demonstrating that these images are of high quality compared to those of many other cryomicroscopy studies [20].

As a test of the correspondence between our reconstruction and the reference model, we again calculated correlations between the map and various models built with different protofilament rotational angles. The results (data not shown) demonstrate that the rotation used in the model indeed gives the best fit to the result. To see that the choice of the model did not bias the reconstruction toward that model, we used a new model with protofilaments rotated 90° as the reference in computing a new reconstruction. The resulting map was virtually the same as that with the correct model, except for a somewhat higher noise level.

Figure 5 shows a contour plot from one section of the final microtubule map. This representation gives a sense of the signal to noise ratio as well as the wealth of structural details in the map. Sections through adjacent molecules around the microtubule wall represent views of sections spaced 9.4 Å apart in the axial direction. Alpha helices that run both roughly parallel to the axis and within the plane of the section are particularly well resolved. Positions of some of the helices in the tubulin structure are marked.

Figure 6 shows surface-rendered views of the map. Figure 6A is an overall view in which a number of well-

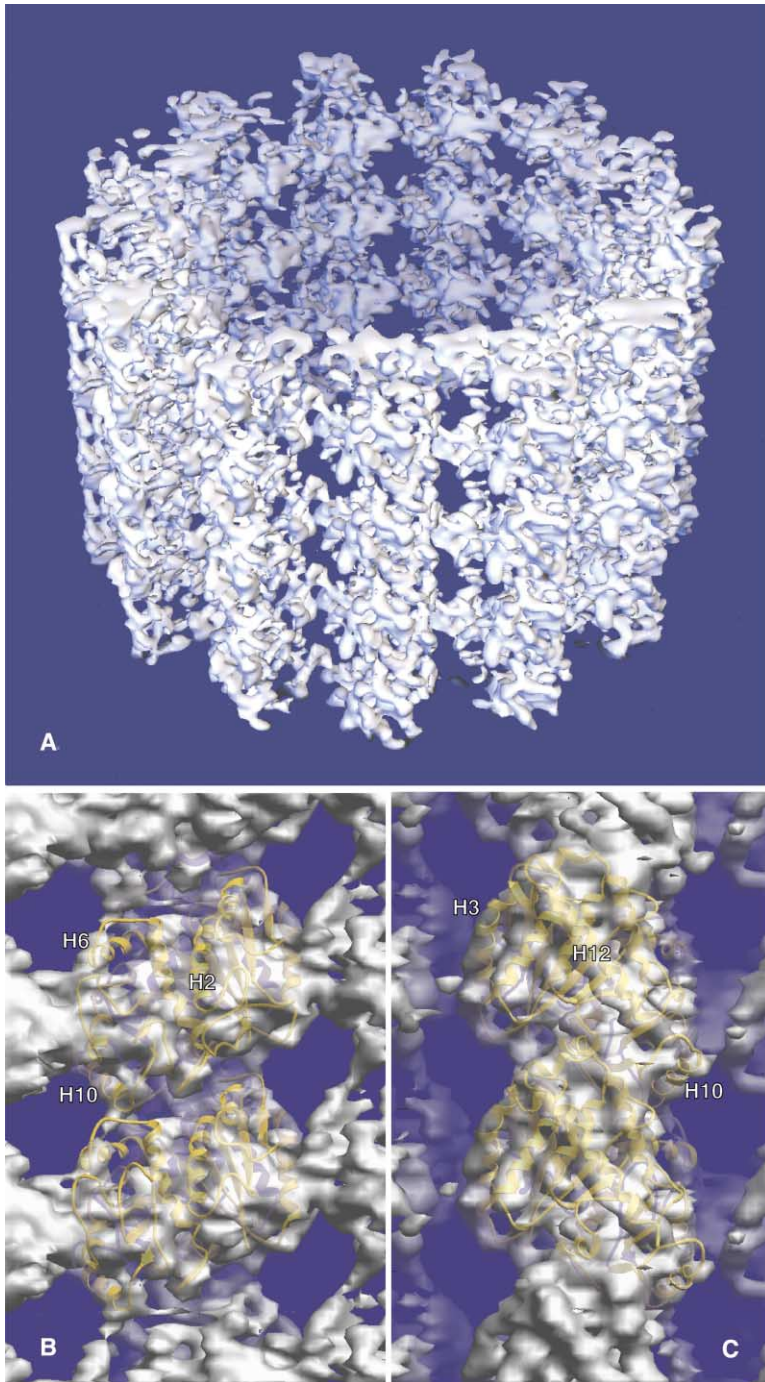


Figure 6. Surface Views of the Map

(A) Overall view, with the plus end of the microtubule toward the top.

(B and C) Views from the inside and outside, respectively, with a ribbon model of the refined atomic structure [3] (Protein Data Bank ID 1JFF) embedded. Helix numbers are marked to aid in orientation. The figure was prepared with AVS (Advanced Visual Systems, Waltham, MA)

defined, tubular densities can be seen. This level of detail allows docking of the atomic structure of the protein with a very high degree of precision in the position. Figures 6B and 6C are views of one dimer in which a ribbon diagram of the crystal structure has been docked, seen from the inside and outside of the microtubule, respectively. Most of the prominent features of the map correspond to helices of the structure, as marked. Except for helix H6 and the loop that connects it to H7, the ribbon diagram fits well within density at the isosurface level used in this figure.

To quantify the accuracy of this docking, we calculated the crosscorrelation between the map and a model density computed from the crystal structure as the model was moved around within the map, as described earlier [13]. As shown in Figure 3, the rotational angle is well defined to about $\pm 2^\circ$, while, in x, y, and z, the position is accurate to about 1 Å (data not shown).

The Fourier shell correlation (FSC) and differential phase residual (DPR) are commonly used as measures of resolution in single particle reconstructions by electron microscopy [21, 22]. We have calculated these mea-

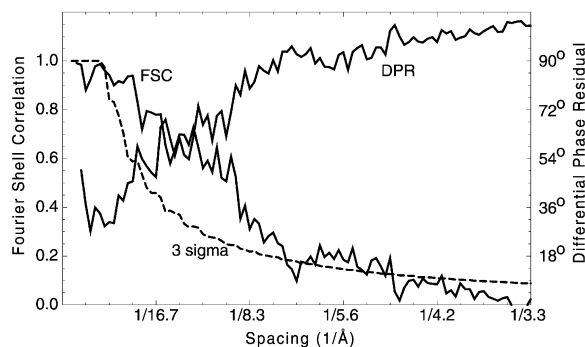


Figure 7. Evaluation of Resolution and Similarity to Model
Fourier shell correlation (FSC) and differential phase residual (DPR) are calculated between the resultant map and the model built from the crystal structure. The dashed curve represents the expected value of the FSC in the absence of signal. For random data, the DPR reaches 104° [21].

asures of similarity between the experimental density map and the reference model derived from the crystal structure, as shown in Figure 7. The dashed curve indicates the statistically expected error level in the FSC, calculated at 10.8σ , which corresponds to the usual 3σ curve when the 13-fold symmetry is taken into account. The FSC drops to 0.5 at 9 Å resolution and crosses the 3σ curve at 7 Å, giving two similar values for the resolution according to two criteria in common usage. Also, the DPR is below 90° out to about 8 Å, while the value expected for random noise is 104° [23]. We note that these may be overly conservative measures of resolution, since, as discussed below, we find evidence that the tubulin structure is not precisely the same in the microtubule as it is in the crystal.

Discussion

Single-Particle Approach to Microtubule Structure

The application of single-particle methods to microtubules has allowed averaging of a sufficient number of images to produce a density map at a resolution of about 8 Å, within which we can identify much of tubulin's secondary structure. Working at a resolution lower than about 7 Å allows us to ignore the differences between α and β monomers. Even with some anticipated differences between the crystal and microtubule structures, we can use a reference for particle alignment that is constructed from the atomic structure. Since this reference is used for alignment of the image segments, but not the protofilaments within the segments, the model produces no noticeable bias toward itself in the reconstruction process. On the other hand, calculating the FSC between the model and reconstruction gives a conservative estimate for the resolution, since the tubulin conformation used in making the model may be slightly different from the conformation in the microtubule.

Structure of Tubulin in Microtubules Versus that in Zinc Sheets

A detailed comparison of the structures of tubulin within the microtubule and within the Zn sheets used to obtain

the atomic model can be obtained by docking the crystal structure of the tubulin dimer within our 8 Å microtubule map. At this resolution, α helices are readily visible, making docking highly precise. Figures 8A and 8B show areas of well-defined density (red mesh) that enclose α -helical segments (blue backbone traces). These regions provide strong constraints for placement of the atomic model and demonstrate that the conformation of tubulin is overall the same in the Zn sheets and microtubules.

Figure 9A is a view from the inside of the microtubule, including the region of the lateral interface between protofilaments. The M loop, which was previously identified as a critical element in the interface [13], corresponds to well-defined density in the present microtubule reconstruction. However, there are small, but significant, differences in this region between microtubules and Zn sheets. The upper part of the M loop appears to be shifted downward in the microtubule structure. While this change is about at the limit of our detectability with the present resolution and signal to noise ratio, conformational differences in this region are expected and are of particular interest, since the interprotofilament interactions are different in the sheets and microtubules. Downward shifting of part of this loop would result in the widening of the "holes" in the microtubule wall. This is potentially relevant to understanding the rapid access of ligands to the luminal surface of the microtubule (see below).

Our microtubule reconstruction shows a clear density in the region that is occupied in the atomic model by Taxol in β -tubulin and the B9-B10 loop in α -tubulin. The location of Taxol near the M loop suggested that its stabilizing effect is likely to involve the inducement or stabilization of an M loop conformation that favors the interprotofilament interaction [13, 24, 25]. In Zn sheets, the M loop interacts across the interface with helices H12 and H5, while, in microtubules, it interacts with helix H3 and the long, N-terminal H1-S2 loop. Although the elements with which the M loop interacts are completely different in Zn sheets and microtubules [3], Taxol has the same stabilizing effect on both. Thus, it is likely that the M loop has been fixed by Taxol in similar, extended conformations in both of these polymers.

In Zn sheets, the H1-S2 loop is poorly resolved. In the electron crystallographic studies of the sheets, this long loop was in direct contact with the carbon support in every second protofilament along the sheet. This may have introduced variable distortions resulting in loss of resolution, although the possibility that the loop was disordered to start with cannot be discarded. In our recent refined structure of tubulin, we could trace this loop for β -tubulin, but not for α -tubulin [3]. In the present microtubule map, there is very strong density for this part of the structure, as has been seen in previous, lower-resolution reconstructions [6–10, 14]. The strong density in this region is most likely due to the stabilization of the H1-S2 loop through its interaction with the M loop of the neighboring molecule (also notice that, in this case, there was no carbon support and that this region is close to the lumen and far from any surface that could produce distortion during specimen preparation).

Our studies identify this N-terminal loop as a principal

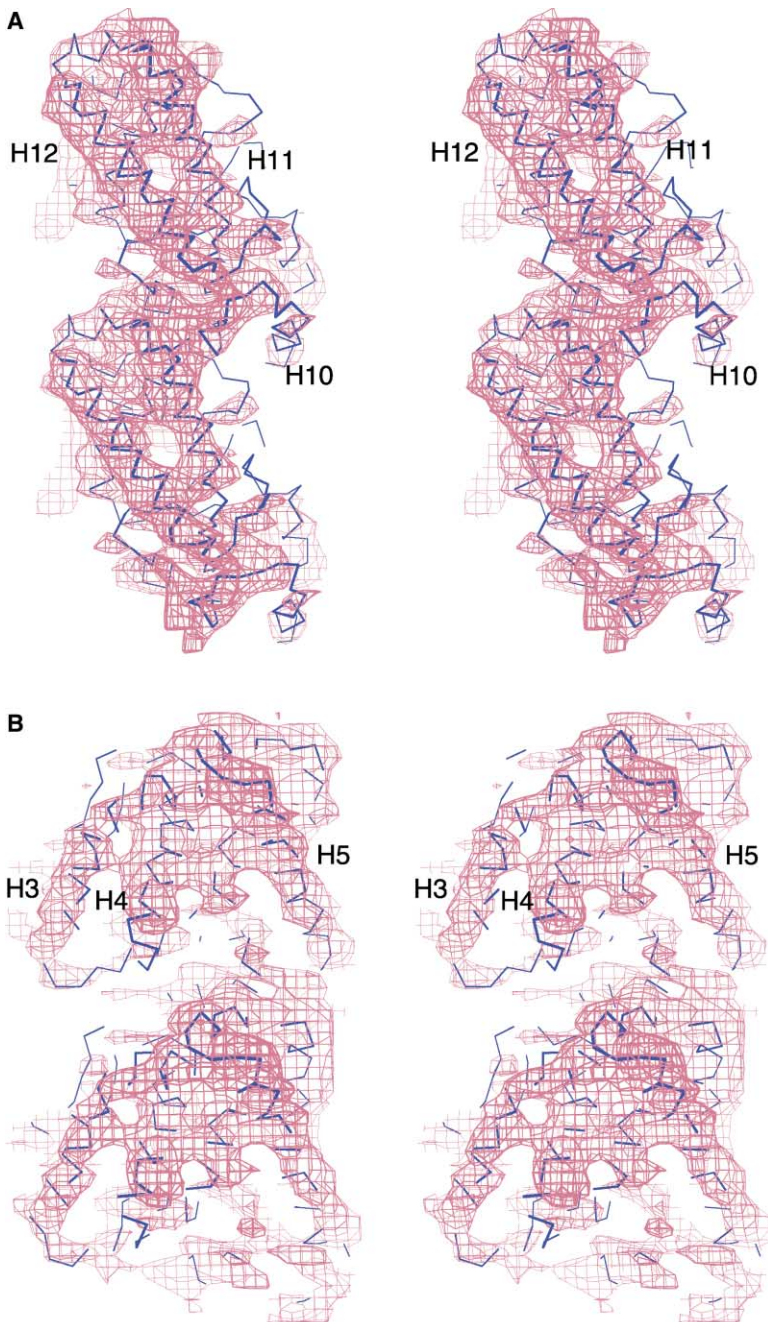


Figure 8. Two Views from the Outside of the Microtubule Showing the Fit between the Tubulin Structure and the Map

(A) The region including helices H11 and H12.
(B) The region of helices H3, H4, and H5.

partner of the M loop for contacts between protofilaments in the microtubule. Figure 9B is an axial view of the interface between protofilaments. The density corresponding to H3 is farther from the M loop than in our previous docking, resulting from a rotation of the protofilament by about 5° from the orientation described earlier. This orientation, similar to what has been found in more recent work [10, 14, 26], suggests a more peripheral role for H3 in the formation of the lateral interface. Figure 10 shows the interacting surfaces of two crystal structures docked into adjacent protofilaments. They are colored to show charge and hydrophobicity of the side chains at the surface. Although some change in

the precise conformation of both the M loop and the H1-S2 loop are expected in the microtubule, the figure shows that there is a fair degree of complementarity across the interface.

Previously, we had attributed much of the interprotofilament interaction to helix H3. We now find that the N-terminal H1-S2 loop (N loop) plays a more substantive role. This may help to understand some features of microtubule dynamics. While most of the differences among tubulin isotypes are found in the C terminus, there is a cluster of residues in the N loop region that vary among β tubulin isotypes. This cluster is positioned just at the region of the interprotofilament interaction

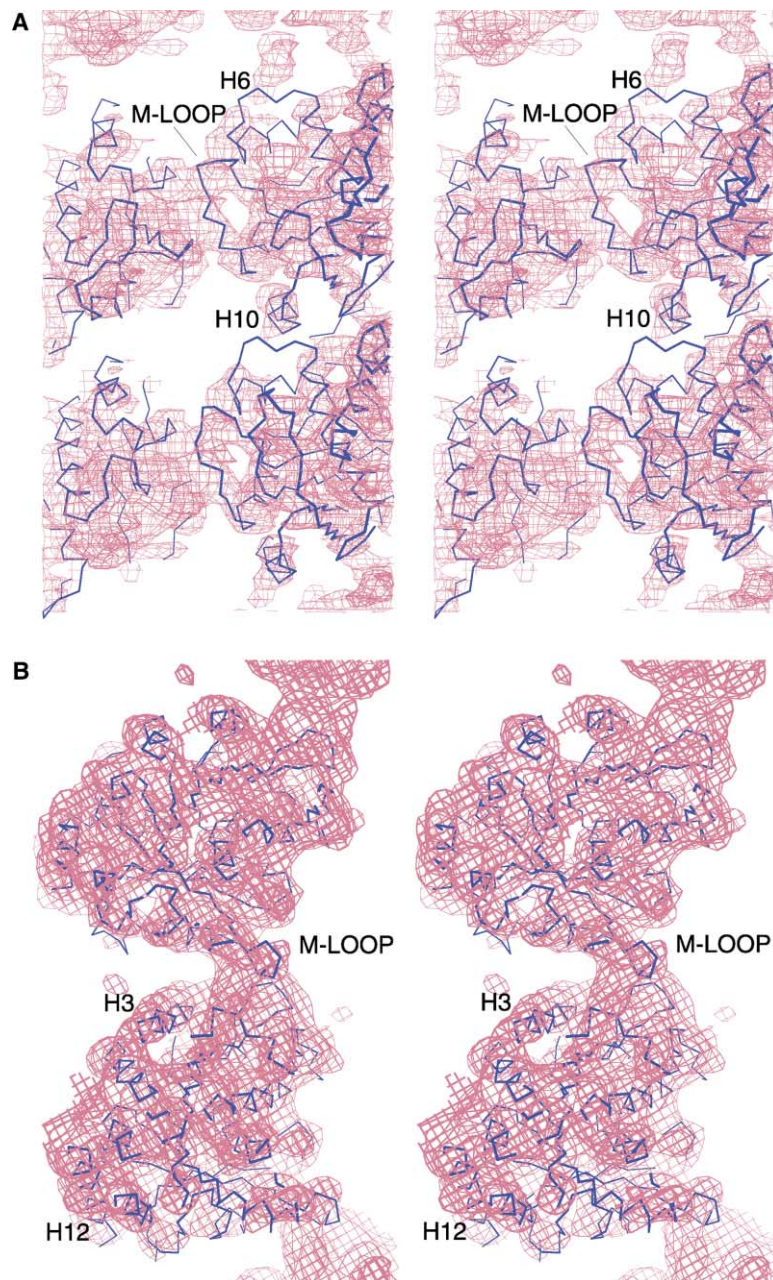


Figure 9. Detail of the Fit between the Tubulin Structure and the Map

(A) A view from the inside of the microtubule, showing the M- and N-terminal loop region. (B) A view from the plus end showing interprotofilament interactions.

with the M loop, as shown in Figure 10, and it is possible that the amino acid differences at this point play a critical role in determining the different dynamic properties of the purified isotypes [27] as well as the different sensitivities to drugs, such as Taxol [28]. Relating the isotype sequence differences to the different responses to Taxol, in particular, supports the hypothesis that a major part of the effect of Taxol lies in stabilizing a conformation of the M loop that favors the interprotofilament interaction. The proximity of these isotype-specific residues to the Taxol binding site suggests that it may eventually be possible to develop isotype-specific drugs that would overcome the clinical problem of drug resistance that arises from alterations in tubulin isotype levels during treatment [29].

Figures 5, 9A, and 10 show that the interaction between protofilaments occurs mainly toward the luminal side of the apposing protofilament surfaces. With the changes in angle that accompany increasing the number of protofilaments in a microtubule, the interactions involving helix H3, H10, and other elements at higher radius become more pronounced. While the increasing surface area involved may contribute to enhanced stability of this interaction, the upper limit in protofilament number may be set by the requirement to maintain the angle small enough to avoid stress on the M loop-H1-S2 loop interaction.

The most prominent structural difference between the conformation of tubulin in our microtubule structure and the crystallographic model appears at the end of the

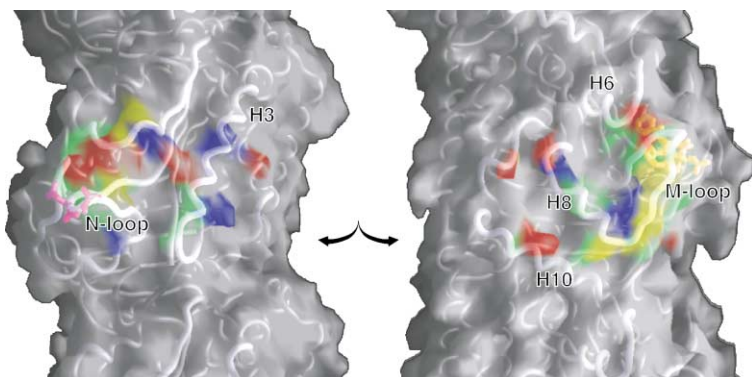


Figure 10. Surface of Interaction between Protofilaments

The protofilaments containing a backbone worm representation of the crystal structure are rotated 90° apart, as indicated, to show the M loop with helices H6, H9, and H10 (right) and the N-terminal loop and H3 (left). Regions of each surface of β tubulin within 4 Å of the opposite surface are colored as follows: red, positively charged side chains; blue, negatively charged side chains; yellow, hydrophobic residues; green, uncharged polar residues. Residues 57–59 are indicated in magenta on the left panel, and Taxol is shown in orange behind the M loop in the right panel. This figure was prepared with Grasp [36].

nucleotide binding region, in helix H6 and the H6-H7 loop. The N-terminal end of H6 is directly in contact with the guanine moiety of the nucleotide, and the helix runs away from the nucleotide binding domain and toward the second domain. Thus, this helix is part of a peptide segment that has been proposed to act as a hinge, allowing the nucleotide binding domain and the intermediate domain to rotate after GTP hydrolysis [24, 30]. In the crystal structure, H6 and the loop connecting it to the core H7 helix form a small module that is mostly separated from the main body of the monomer. In the Zn sheets this small domain was well resolved [2], being stabilized by contacts with helix H4 of the adjacent molecule and, more importantly, with the upper three amino acids of the M loop [3]. In the microtubule there is no interaction of this segment across the protofilament interface. Furthermore, the microtubule structure suggests that the upper part of the M loop is shifted downward, away from H6. The loss of density for H6 and the following loop may be a consequence of this apparent lack of stabilizing contact. Thus, it seems that this region may be flexible in the microtubule. Alternatively, there may be some displacement that follows nucleotide hydrolysis in β -tubulin, resulting in different positions for this segment in the two monomers, making the density weaker when averaged. This hypothesis agrees with the notion that this region is key in larger conformational differences between the GTP- and GDP-bound forms of tubulin, even though it is positioned at the end of the nucleotide away from the phosphates [24], but is not supported by the crystal structure, in which this region appears well defined and very similar for both GTP-bound α -tubulin and GDP-bound β -tubulin.

In conclusion, it seems that, in Zn sheets, contacts between the M loop and helix H6 within the same molecule may stabilize both of them. In microtubules, the M loop conformation is slightly different, so it loses the contact with H6, rendering the helix more mobile. As an alternative, the lack of the contact of H6 with the adjacent protofilament may result in a flexible H6 region that then does not effectively interact with the M loop, which then moves down in the microtubule structure. In any case, a flexible H6 module would increase the effective size of the holes in the microtubule wall, enhancing the diffusion of small ligands into the microtubule lumen.

It has been a puzzle that, while Taxol binds to the inside of the microtubule, its binding and exchange rates

are extremely rapid. Diaz et al. [31] initially proposed that Taxol gets into the microtubule through transient openings between protofilaments but later saw the same binding speed to microtubules that had been crosslinked and were not expected to open [32]. The apparent mobility of the H6 module in our present microtubule structure has the consequence that the pore in the wall is large enough, approximately 17 Å across, to allow the passage of molecules of the size of Taxol.

The small shift of the M loop in microtubules relative to the Zn sheets reflects some of the polymorphism in tubulin polymers. It has been reported that, when the Zn sheets roll up to form macro tubes, at slightly higher pH, there is an axial offset of about 6 Å between protofilaments [33]. Also, a slight shift in the relative positions of the adjacent protofilaments was observed when Taxol was added to reassembled microtubules [34]. These effects could all be attributed to small shifts in the M loop.

Biological Implications

The structural design of the microtubule is remarkable in terms of its biological functions. The surface displays a surprisingly large number of binding sites, with numerous MAPs binding to the outside surface and a multitude of small ligands binding to the inside [35]. Our present understanding is that, normally, dynamics are regulated by proteins that interact with the outside surface or the ends of the microtubule, while the natural compounds that can pass through the wall to bind on the inner surface are generally poisons that may be used in chemical defense. Further characterization of microtubule structure and these binding sites should play an important role in enhancing our understanding of cell cycle control.

The success of our approach to microtubule structure shows that tubular or helical structures can, in some cases, be better treated as strings of single particles than as helices. This method has great potential for other ordered protein assemblies where distortions or other effects limit the use of helical methods. The essential requirement is that the image be segmented into regions that are large enough so that they can be accurately aligned, but small enough to avoid distortions within the segments. With the greatly improved resolution of the present map, we have extended our understanding of

the interactions that govern microtubule stability and dynamics. In further studies on microtubules, the methodology serves as a basis for studying the interactions with other proteins or structures, such as the microtubule doublet. To reach higher resolution or to work with proteins that decorate the dimer, rather than both monomers, we will need to be able to distinguish between the α and β monomers. The presence of a seam in the structure will preclude the 13-fold rotational averaging we have done here, but, otherwise, the same principles apply.

Experimental Procedures

Tubulin was obtained from Cytoskeleton (Denver, CO). Microtubules were polymerized with tubulin at 5 mg/ml in G-PME buffer (80 mM PIPES, 1 mM EGTA, 1 mM $MgCl_2$, and 1 mM GTP [pH 6.8]) in the presence of 50 μ M Taxol. After incubation for about 30 min at 37°C, samples were applied to glow-discharged holey carbon films and plunge-frozen in liquid ethane. Images were recorded at a magnification of 60,000 on Kodak SO-163 film in a JEOL-4000 electron microscope operating at 400 kV. About half of the images were taken with a defocus of 0.8–1.2 μ m, and about half were taken with a defocus 1.5–2.8 μ m. Negatives were examined on an optical bench to identify microtubules showing good resolution. The main criterion for selection was the visibility of the layer line at 20 Å resolution. Selected areas enclosing microtubules were digitized on a PDS-1010M densitometer with a step size of 10 μ m, corresponding to 1.6 Å on the specimen. Scan sizes were 500 \times 500–8000 pixels. All image processing was carried out with the SPIDER package [19].

Each microtubule was boxed into small segments of 320 \times 320 pixels, including a length of 13 monomers. In each segment, there are a total of 13 \times 13, or 169, tubulin monomers, with a total molecular mass of 8.5 MDa.

Acknowledgments

This work has been supported by NIH grants GM40633 (K.H.D.), GM26357, and GM35433 (D.J.D.), a UC Miller Visiting Professorship (D.J.D.), and the Office of Health and Environmental Research, US Department of Energy, under contract DE-AC03-76F00098.

Received: February 1, 2002

Revised: May 10, 2002

Accepted: June 20, 2002

References

1. Nogales, E. (2000). Structural insights into microtubule function. *Annu. Rev. Biochem.* 69, 277–302.
2. Nogales, E., Wolf, S.G., and Downing, K.H. (1998). Structure of the $\alpha\beta$ tubulin dimer by electron crystallography. *Nature* 391, 199–203.
3. Löwe, J., Li, H., Downing, K.H., and Nogales, E. (2001). Refined structure of alpha beta-tubulin at 3.5 Å resolution. *J. Mol. Biol.* 313, 1045–1057.
4. Nogales, E., Wolf, S.G., Khan, I.A., Ludueña, R.F., and Downing, K.H. (1995). Structure of tubulin at 6.5 Å and location of the taxol-binding site. *Nature* 375, 424–427.
5. Chrétien, D., and Wade, R. (1991). New data on the microtubule surface lattice. *Biol. Cell* 71, 161–174.
6. Sosa, H., Dias, D.P., Hoenger, A., Whittaker, M., Wilson-Kubalek, E., Sablin, E., Fletterick, R.J., Vale, R.D., and Milligan, R.A. (1997). A model for the microtubule-Ncd motor protein complex obtained by cryo-electron microscopy and image analysis. *Cell* 90, 217–224.
7. Hoenger, A., Sack, S., Thormahlen, M., Marx, A., Muller, J., Gross, H., and Mandelkow, E. (1998). Image reconstructions of microtubules decorated with monomeric and dimeric kinesins: comparison with x-ray structure and implications for motility. *J. Cell Biol.* 4, 419–430.
8. Arnal, I., Metoz, F., DeBonis, S., and Wade, R.H. (1996). Three-dimensional structure of functional motor proteins on microtubules. *Curr. Biol.* 6, 1265–1270.
9. Hirose, K., Amos, W.B., Lockhart, A., Cross, R.A., and Amos, L.A. (1997). Three-dimensional cryoelectron microscopy of 16-prot filament microtubules: structure, polarity and interaction with motor proteins. *J. Struct. Biol.* 118, 140–148.
10. Kikkawa, M., Okada, Y., and Hirokawa, N. (2000). 15 Å resolution model of the monomeric kinesin motor, KIF1A. *Cell* 100, 241–252.
11. Metoz, F., Arnal, I., and Wade, R. (1997). Tomography without tilt: three dimensional imaging of microtubule/motor complexes. *J. Struct. Biol.* 118, 159–168.
12. Sosa, H., Hoenger, A., and Milligan, R.A. (1997). Three different approaches for calculating the three dimensional structure of microtubules decorated with kinesin motor proteins. *J. Struct. Biol.* 118, 149–158.
13. Nogales, E., Whittaker, M., Milligan, R.A., and Downing, K.H. (1999). High-resolution model of the microtubule. *Cell* 96, 79–88.
14. Meurer-Grob, P., Kasparian, J., and Wade, R.H. (2001). Microtubule structure at improved resolution. *Biochemistry* 40, 8000–8008.
15. Chrétien, D., Metoz, F., Verde, F., Karsenti, E., and Wade, R.H. (1992). Lattice defects in microtubules: protofilament numbers vary within individual microtubules. *J. Cell Biol.* 117, 1031–1040.
16. Egelman, E.G. (1986). An algorithm for straightening images of curved filamentous structures. *Ultramicroscopy* 19, 367–373.
17. Radermacher, M. (1994). Three-dimensional reconstruction from random projections: orientational alignment via radon transforms. *Ultramicroscopy* 53, 121–136.
18. Lanzavecchia, S., Bellon, P.L., and Radermacher, M. (1999). Fast and accurate three-dimensional reconstruction from projections with random orientations via radon transforms. *J. Struct. Biol.* 128, 152–164.
19. Frank, J., Radermacher, M., Penczek, P., Zhu, J., Li, Y.H., Ladjadj, M., and Leith, A. (1996). SPIDER and WEB: processing and visualization of images in 3D electron microscopy and related fields. *J. Struct. Biol.* 116, 190–199.
20. Saad, A., Ludtke, S.J., Jakana, J., Rixon, F.J., Tsuruta, H., and Chiu, W. (2001). Fourier amplitude decay of electron cryomicroscopic images of single particles and effects on structure determination. *J. Struct. Biol.* 133, 32–42.
21. Penczek, P.A., Grassucci, R.A., and Frank, J. (1994). The ribosome at improved resolution: new techniques for merging and orientation refinement in 3D cryo-electron microscopy of biological particles. *Ultramicroscopy* 53, 251–270.
22. van Heel, M., Gowen, B., Matadeen, R., Orlove, E.V., Finn, R., Pape, T., Cohen, D., Start, H., Schmidt, R., Schatz, M., et al. (2000). Single-particle electron microscopy: towards atomic resolution. *Q. Rev. Biophys.* 33, 307–369.
23. Frank, J., Verschoor, A., and Boublik, M. (1981). Computer averaging of electron micrographs of 40S ribosomal subunits. *Science* 214, 1353–1355.
24. Amos, L., and Löwe, J. (1999). How Taxol stabilizes microtubule structure. *Chem. Biol.* 6, R65–R69.
25. Snyder, J.P., Nettles, J.H., Cornett, B., Downing, K.H., and Nogales, E. (2001). The binding conformation of Taxol in beta-tubulin: a model based on electron crystallographic density. *Proc. Natl. Acad. Sci. USA* 98, 5312–5316.
26. Chacon, P., and Wriggers, W. (2002). Multi-resolution contour-based fitting of macromolecular structures. *J. Mol. Biol.* 317, 375–384.
27. Ludueña, R.F. (1998). The multiple forms of tubulin: different gene products and covalent modifications. *Int. Rev. Cytol.* 178, 207–275.
28. Derry, W.B., Wilson, L., Khan, I.A., Ludueña, R.F., and Jordan, M.A. (1997). Taxol differentially modulates the dynamics of microtubules assembled from unfractionated and purified β -tubulin isotypes. *Biochemistry* 36, 3554–3562.
29. Dumontet, C., Duran, G.E., Steger, K.A., Beketicoreskovic, L., and Sikic, B.I. (1996). Resistance mechanisms in human sarcoma mutants derived by single-step exposure to paclitaxel (Taxol). *Cancer Res.* 56, 1091–1097.

30. Erickson, H.P. (1998). Atomic structures of tubulin and FtsZ. *Trends Cell Biol.* *8*, 133–137.
31. Diaz, J.F., Valpuesta, J.M., Chacon, P., Diakun, G., and Andreu, J.M. (1998). Changes in microtubule protofilament number induced by taxol binding to an easily accessible site—internal microtubule dynamics. *J. Biol. Chem.* *273*, 33803–33810.
32. Diaz, J.F., Strobe, R., Engelborghs, Y., Souto, A.A., and Andreu, J.M. (2000). Molecular recognition of Taxol by microtubules—kinetics and thermodynamics of binding of fluorescent Taxol derivatives to an exposed site. *J. Biol. Chem.* *275*, 26265–26276.
33. Wolf, S.G., Mosser, G., and Downing, K.H. (1993). Tubulin conformation in zinc-induced sheets and macrotubes. *J. Struct. Biol.* *111*, 190–199.
34. Chrétien, D., Flyvbjerg, H., and Fuller, S.F. (1998). Limited flexibility of the interprotofilament bonds in microtubules assembled from pure tubulin. *Eur. Biophys. J.* *27*, 490–500.
35. Downing, K.H. (2000). Structural basis for the interaction of tubulin with proteins and drugs that affect microtubule dynamics. *Annu. Rev. Cell Dev. Biol.* *16*, 89–111.
36. Nicholls, A., Sharp, K.A., and Honig, B. (1991). Protein folding and association—insights from the interfacial and thermodynamic properties of hydrocarbons. *Proteins Struct. Funct. Genet.* *11*, 281–296.